ARTICLE

Check for updates

Projected Atlantic overturning slow-down is to be compensated by a strengthened South Atlantic subtropical gyre

Fernanda Marcello [1 ✉], Marcos Tonelli [1,2], Bruno Ferrero [1] & Ilana Wainer [1]

The upper limb of the Atlantic meridional overturning circulation brings shallow interocean contributions to replenish the North Atlantic export of deepwaters. It is primarily formed in the southern South Atlantic where the converging entrainment of Pacific and Indian Ocean waters meet and incorporate into the South Atlantic subtropical gyre. Here, we use Community Earth System Model 1 Large Ensemble simulation results along 1920–2100 to investigate the response of the Atlantic meridional overturning circulation upper limb and the South Atlantic subtropical gyre to future human-induced climate warming under business-as-usual greenhouse gas emissions. In terms of flow redistribution, we find that the Atlantic meridional overturning circulation upper limb weakens not because less waters are being imported from the Pacific and Indian basins — but because waters are being mostly directed to recirculate in the southwestern portion of a distorted South Atlantic subtropical gyre, turning back southward after reaching the South Atlantic western boundary.

[1] Oceanographic Institute of the University of São Paulo, Department of Physical Oceanography, São Paulo, SP, Brazil. [2] Admiral Paulo Moreira Institute for Marine Studies, Arraial do Cabo, RJ, Brazil. ✉email: fernanda.marcello@usp.br

From the southeastern corner of the South Atlantic (SA) towards the subpolar North Atlantic, the upper limb of the Atlantic Meridional Overturning Circulation (AMOC) flows along shallow and intermediate pathways to feed deep water formation in order to meet mass conservation constraints, as part of the global overturning circulation (GOC) — a system that dictates how the ocean affects the global climate, redistributing important properties such as carbon and heat[1–4].

Both changes in the amount of contributions from the Indian warm water[5–7] or the Pacific cold water[8,9] routes — the two contrasting main sources for the near-surface upper limb flow of the AMOC[10–12] — or changes in how these water masses are circulated and transformed within the SA itself[13–15], might influence deep water convection and therefore affect overturning variability and strength[16–20].

The northward AMOC upper limb takes place in the upper ~1000–1500 m of the ocean, and therefore strongly interacts with major wind-driven current systems such as the subtropical gyres and the circumpolar current, prior to arriving at deep water formation areas[21] (Fig. 1a). More specifically, waters from the cold water route enter the southwestern SA basin through the Drake Passage (DP) with the Antarctic Circumpolar Current-Malvinas Current (ACC-MC) system and merge into the South Atlantic Current (SAC) — delimiting the South Atlantic subtropical gyre (SASG)[22] to the south. By reaching the eastern corner of the basin, the flow meets with contributions from the Agulhas leakage (AL), the warm water route. From there on, a blend of cold and warm water routes is incorporated into the northwestward anticyclonic loop of the SASG[23]: the Benguela Current-southern South Equatorial Current (BeC-sSEC) system, until reaching the South American coast, at the SA western boundary.

Up to this point, the overturning circulation return flow is superposed to the wind-driven subtropical gyre circulation in the SA, meaning that the AMOC upper limb and the SASG are coupled large-scale circulation features, which decouple when the zonal sSEC flow is forced to bifurcate[24] at the northern boundary of the SASG, originating two opposing western boundary currents (WBCs): the poleward Brazil Current (BC), closing the subtropical gyre circulation, and the equatorward North Brazil Undercurrent-North Brazil Current (NBUC-NBC) system, continuing to the upper ocean return flow of the AMOC[25–30].

Even though the AMOC is a highly non-linear system[31] and its response to human-induced global warming is far from being fully resolved[32–55], the majority of the current generation climate models project a future AMOC decline[56–58].

Meanwhile, systematic wind-related changes[59] have been reported in upper ocean gyre circulations[60–66] of both the Pacific[67–73] and Indo-Atlantic[74–78] basins, linked to a spin-up and poleward expansion of the Southern Hemisphere supergyre (SHSG)[79–83] — an interbasin feature that represents the connectivity between all three southern subtropical gyres, linking the South Pacific, SA and Indian oceans[20,84,85]. These changes are also uncertain, owing to the opposing effects of increasing CO_2 and ozone recovery after 2000[86], that are further complicated by chaotic natural climate variability[87] — which might reinforce or weaken ongoing trends, or either combine to even out dominant changes[88,89]. Still, recent studies have described ongoing Southern Hemisphere (SH) ocean circulation changes in association to shifted wind-patterns[90–98], suggesting that the poleward intensification of SH surface westerlies is projected to continue in the future under a high emission scenario in spite of the projected stratospheric ozone recovery, once future trends will likely be dominated by the increasing CO_2 effect[99,100]. It is concluded with medium confidence that WBCs and subtropical gyres have shifted poleward since 1993 in response to a poleward shift of the multi-basin scale wind stress curl, due to anthropogenic global warming[52,57].
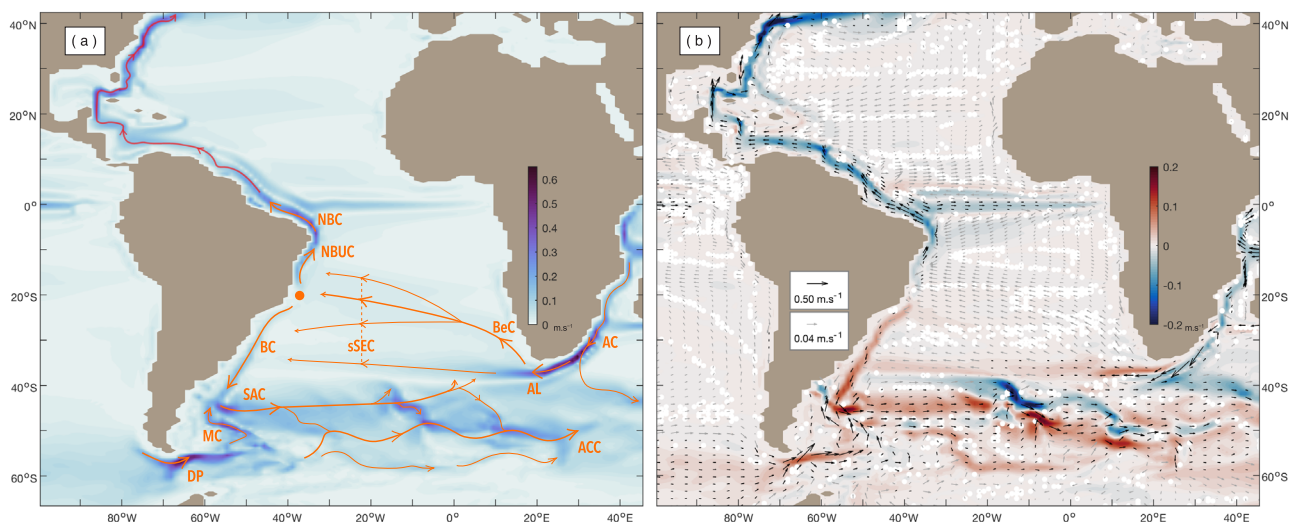

Fig. 1 Schematic of the South Atlantic circulation and projected changes in the transport of ocean currents along the 20th and 21st centuries, as according to the ensemble mean of CESM1-LE simulations. a Mean 1920–2100 flow field represented by the absolute magnitude of horizontal velocities averaged over the upper 985-m layer (background shading) superposed by a schematic of the South Atlantic circulation including the oceanographic features and currents mentioned in the text. DP, Drake Passage; MC, Malvinas Current; SAC, South Atlantic Current; ACC, Antarctic Circumpolar Current; AC, Agulhas Current; AL, Agulhas Leakage; BeC, Benguela Current; sSEC, southern South Equatorial Current; NBUC, North Brazil Undercurrent; NBC, North Brazil Current; BC, Brazil Current. The orange circle at ~20°S, 40°W represents the mean sSEC bifurcation latitude. **b** Ocean currents getting faster (red)/ slower (blue) from 1920 to 2100. Superposing vectors denote the 1920–2100 mean horizontal velocities averaged over the upper 985-m layer, giving a perspective of the mean flow intensity and direction. The background shading represents the total trends along 1920–2100 of the absolute magnitude of upper 985 m horizontal velocity anomalies with respect to the 1920–1970 base period. Black (gray) vectors are plotted over regions where the absolute velocity magnitude is above (below) the mean value (0.035 m.s^{-1}), for clarity. Gray vectors are scaled by a factor of 50, in comparison with black vectors. Red (blue) indicates regions where velocity magnitudes tend to increase (decrease). Grid points where trends are not statistically significant at the 95% confidence level are marked with white dots.

In a time when human activity is forcing substantial changes to the Earth system, a comprehensive understanding of the interplay between different climate components is needed, further considering the full three-dimensionality of the ocean circulation and its changes[101]. Both the SASG and the AMOC upper limb are influenced by wind and buoyancy forcings interacting in non-linear ways within the SA basin[102]. Therefore, variations in the horizontal subtropical gyre circulation may reflect variations in the upper limb flow structure and vice-versa. The potential slowdown of the modern and future AMOC is likely to extend all the way into the SA[103], while, at the same time, AMOC anomalies observed in the North Atlantic can either be of local origin or originate upstream in the SA and beyond[102,104,105].

This study investigates how upper-ocean circulation changes are communicated along the SA basin, from up- to downstream the pathways which compose the AMOC upper limb and the SASG. Our goal is to assess how integrated changes in high-latitude overturning and hemispheric-scale atmospheric forcing are to be reflected along these main circulation routes, according to the simulation results of the Community Earth System Model 1 Large Ensemble (CESM1- LE[106]) with future projections under the high-end Representative Concentration Pathway 8.5 (RCP8.5) — the most aggressive yet most realistic scenario, which accounts for the largest additional amount of energy in Earth's climate system by 2100, relative to pre-industrial levels[107]. Beyond natural random climate variability[87], the resulting climate change response is represented by the CESM1-LE 40-member ensemble mean[108], yielding a spatio-temporal pattern of simulated and projected changes in the large-scale SA circulation.

We find a projected end of 21st century circulation change pattern which features a stronger southwestern SASG circulation, at the expense of a weakened northward advection downstream the AMOC upper limb — in which Pacific and Indian Ocean contributions are not diminished, as commonly speculated. The sluggish oceanic transport to the north also contrasts with enhanced Southern Ocean eastward transports along the ACC. These alterations in flow redistribution are accompanied by structural changes in the SASG spatial configuration, which are heterogeneous across the horizontal-depth plane. Moreover, anomalous wind and sea surface height patterns bear the imprints of the oceanic circulation response, supporting the existing literature on SH climate trends: as a consequence of global warming, a major reorganization of ocean dynamics is expected, with a spin-up and poleward expansion of the midlatitude southern seas induced by shifts in the extratropical atmospheric field. Besides potentially compromising the subtropical gyre transport of mass, heat, nutrients and carbon across boundaries[109–113], these results might translate into changes in fundamental thermohaline properties involved in the GOC[114–116].

Results
Overview of projected circulation changes. The pathways which compose the AMOC upper limb and the SASG circulation are pictured through the mean horizontal flow field, represented by superposing vectors in Fig. 1b and their projected change is depicted by the background color shading, indicating where the mean flow tends to strengthen (red) or weaken (blue). Following the up- to downstream flow direction, increasing current velocity trends are found from the DP region into the SA via the MC, and then to the east marking an intensified SAC up to ~20°W; past this longitude, eastward flows are characterized by a complex interplay between the SAC to the north and the ACC to the south[10,117,118] — where the southern ACC transport seems to be favored. The southward Agulhas Current (AC) along the eastern coast of Africa and its retroflection loop back into the Indian

Ocean are marked with decreasing trends. In turn, the AL into the SA increases — mainly along a straight westward path extending up to the opposite side of the basin along ~37°S and building up to the southern termination of the BC, off the South American coast.

The total broad westward flow crossing the SA — from the basin interior to the SASG northern boundary — brings the sSEC waters that eventually spread out meridionally along the South American coast, feeding into the equatorward NBUC and the poleward BC. These diverging western boundary flows display opposing trends straddling the sSEC bifurcation region (~20°–25°S, Fig. 1b): while the southward BC is projected to strengthen, the NBUC exhibits conspicuous negative trends — which expand downstream the AMOC upper limb, all the way into the subpolar North Atlantic.

Changes in up- to downstream ocean current transports. The derived volume transports of ocean currents in specific locations confirm the aforementioned change pattern, further revealing complementary details concerning these circulation changes (Fig. 2). Hereafter in this section, the trends in volume transports (Fig. 2c–e) associated with numbered boxes and transects (Fig. 2a, b) are described. The sign convention is positive upwards for increased transport magnitudes. The vertical profiles associated with boxes and transects are shown in Supplementary Fig. 1, while the values (mean and trends) associated with time series are shown in Supplementary Table 1.

From the Pacific to the Indian sector, across boxes 1–3 (Fig. 2a), eastward transports north (south) of the dashed lines decrease (increase) (Supplementary Figs. 2–4), suggesting an intensification of southerly flows which are associated with the circumnavigating ACC (further discussed in Section 2.4). The decreasing southward transport across box 4 provides indirect evidence for the recent spin-up of the South Pacific subtropical gyre[67,68,72,80] and the SHSG[93]; this is further discussed in the Supplementary Information file (SI), item 11.

Volume transports through the DP (5,6) and into the SA along the MC route (7,8,9) all increase. The BC at its final portion (10) has a strong westward component due to the coastline orientation — which is also projected to increase. The Brazil-Malvinas confluence (BMC) originates the SAC (11) — represented by the eastward (red) core amidst the westward (blue) MC and BC (9 and 10, respectively). Both the increased MC and BC transports add up to form an even stronger SAC.

The sSEC is considered the zonal extension of the BeC, which defines the northern limb of the SASG and is associated with the origins of both the northward NBUC and southward BC[119–122]. There is evidence for a multi-banded sSEC[119,123], and here we define the sSEC as the westward flow between ~10°–40°S, partitioned proportionally between southern, central and northern branches (Fig. 2a — transects 13, 16 and 17, respectively). The AL increase (12) is transmitted further to the west (13 — southern sSEC), while westward transports north of that respectively show no trend at all (16 — central sSEC) or even undergo a steady decrease (17 — northern sSEC). The westward flows through transects 13 and 16 are more likely to feed the southward BC, which also increases at its middle and initial portions (14 and 15, respectively). The declining westward flow through transect 17, in turn, is likely to feed the northward NBUC-NBC system — which undergoes a substantial decrease (18–20).

Hence, the westward transport along the northernmost boundary of the SASG (northern sSEC, 17) is decreasing and consequently compromising the supply of waters to the flow leaving the subtropical gyre to the north, along the AMOC upper limb extension towards the equator (18-20). Although westward flows along the gyre northern boundary just south of that are not
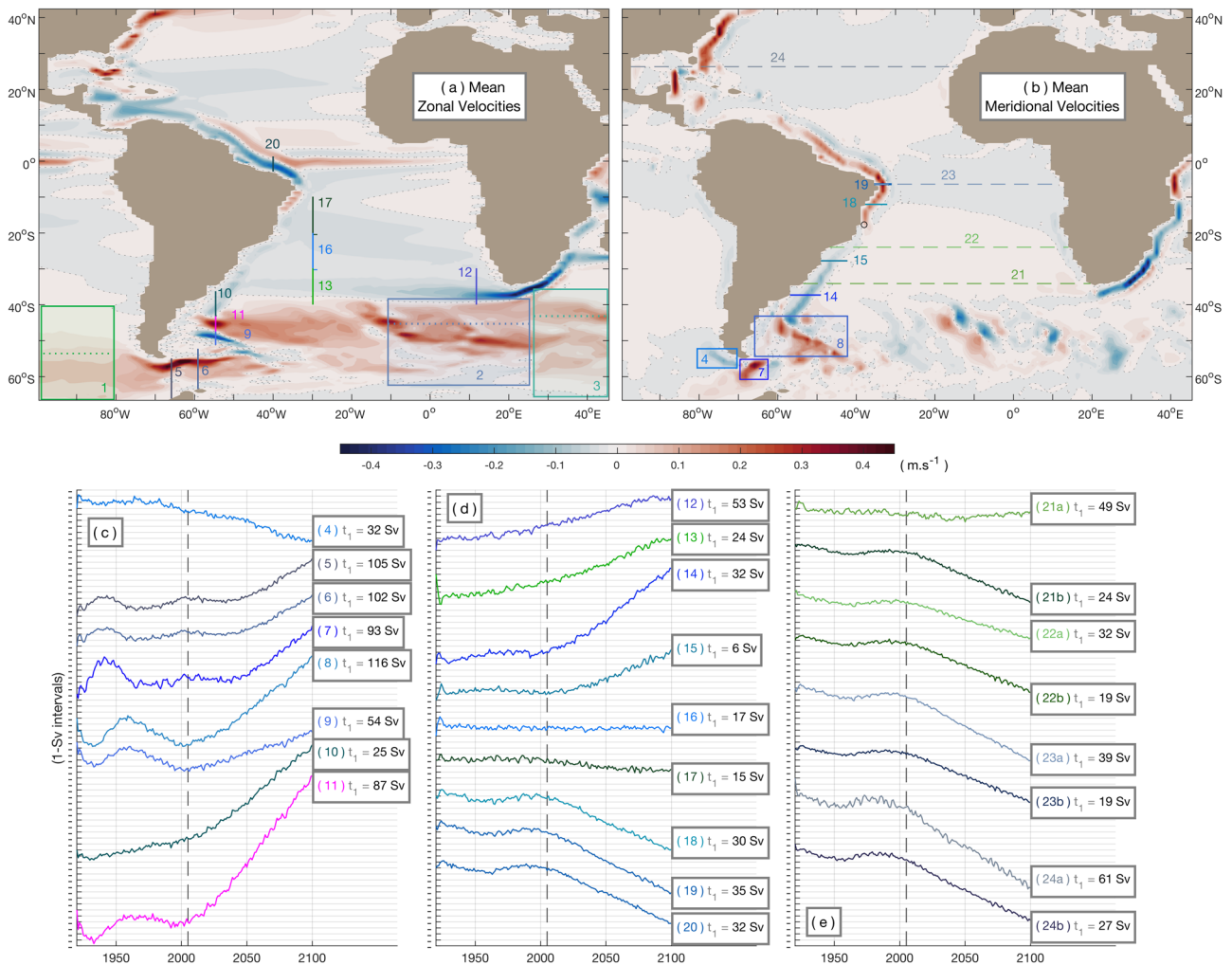
Fig. 2 Changes in volume transports along 1920–2100. Mean zonal (**a**) and meridional (**b**) velocity fields over 1920–2100, averaged over the upper 985-m of the ocean. In both panels, red represents positive (eastward/northward), while blue represents negative (westward/southward) velocities. Dotted gray contours indicate the zero zonal/meridional velocity line. The regions where zonal and meridional volume transports were derived are shown through boxes and transects, whose colors and numbers correspond to those on panels (**c–e**) and on Supplementary Fig. 1 (which shows the vertical profiles associated with boxes/transects). The volume transport time series (**c–e**) are integrated over the upper 985-m layer (slightly above 1-km) across transects and boxes (in the latter case, representing the mean transport along cross-sectional ranges of the boxes). Only MOC streamfunction time series (time series 21b-24b) are vertically integrated up to the depth of transition between north- and southward zonally integrated meridional velocities. When deriving eastward/northward (westward/southward) volume transports, only positive (negative) velocity values are taken into account, to avoid counterflow interference — with exception of MOC streamfunction time series (21b-24b). Panels **c–e** are standardized in length and their y-axis (positive upwards) varies in 1-Sverdrup intervals (1 Sv = 10^6 m^3.s^{-1}). The legends indicate the value corresponding to the first time-step (year of 1920) in each time series (t_1). The gray dashed vertical line marks the transition from the historical (1920–2005) to the RCP8.5 (2006–2100) period. Time series mean and trend values are displayed in Supplementary Table 1.

decreasing (central sSEC, 16 — flat time series), it is suggested that a major amount of the subtropical waters brought to the western boundary across the whole sSEC is being destined to join the BC flow to the south, which is already strengthened at 28°S (15), near its site of origin — where it is considered to be weak and shallow when compared to its downstream extension at higher latitudes[124] (for instance, compare the shallow BC core on Supplementary Fig. 1j, at 28 °S, with the deep ones on Supplementary Fig. 1i and 1f, at 37°S and 55°W, respectively; and its modest mean transport of 7.2 Sv in contrast with 33.7 Sv at 37°S, Supplementary Table 1). Thus, even near-equatorial zonal current systems that are commonly fed by the sSEC and subsequently end up contributing to the northward NBC flow[22,125] get deprived of the supply from these subtropical waters and tend to weaken (see negative anomalies around the Equator on Fig. 1b). For these reasons, the BC transport is

notably increased already at 28°S (15) while the NBUC transport markedly weakens from 12°S (18) northward. Further south, the AL-southern sSEC system (12,13) reinforces the BC flow (14, 10) up to its ultimate fate. The dynamics and mechanisms influencing the reorganization of these gyre pathways are discussed later.

Time series 21–24 refer to zonally integrated meridional transports in the Atlantic basin, across four sections from 34°S to 26.5°N (transbasin vertical profiles shown in Fig. 3a–d). However, time series 21a-24a account only for northward flows (discounting southward returning flows), different from time series 21b-24b, which represent classic AMOC streamfunctions in the depth space. Interestingly, among 21–24 only time series 21a — i.e., northward transports across 34°S — does not follow a decreasing trend. The reason is that, at this latitude, the northward component of the strengthened AL-BeC-sSEC system acts to sustain these transbasin transports, hampering a zonally integrated transport
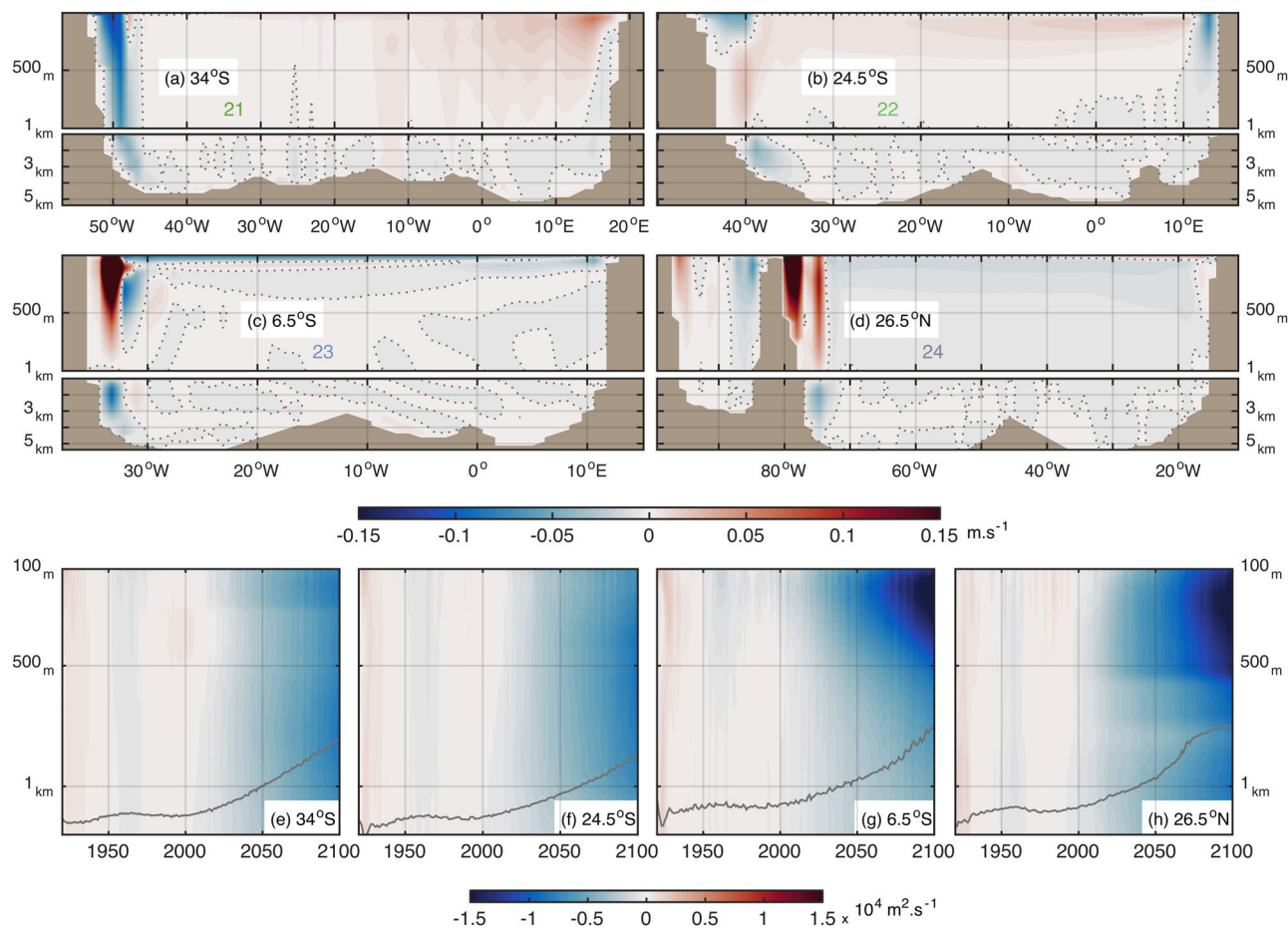
Fig. 3 Projected weakening of the AMOC upper limb from 34°S to 26.5°N. a–d Transbasin meridional velocity profiles (1920–2100 mean) at 34°S, 24.5°S, 6.5°S and 26.5°N, respectively. Red (blue) represents mean northward (southward) velocities. **e–h** Hovmoller diagrams of zonally integrated meridional velocity anomalies along transbasin sections corresponding to **a–d**. Blue (red) represents negative/southward (positive/northward) anomalies. The gray filled contour marks the 1920–2100 evolution of the zero meridional velocity line that delimits the lower limit of the AMOC upper limb. The upper 100-m of Hovmoller diagrams are not shown since it reflects near-surface dynamics within the Ekman layer, which are out of our scope.

decrease. However, waters flowing northward across 34°S do not reach any further — at least not up to 24.5°S (22a) (see Fig. 3a, b for reference) –, because they are being mostly recirculated within the SASG, promptly feeding the southern (and to a lesser degree, the central) sSEC south of ∼ 24.5°S, prior to turning poleward and contributing to strengthening the BC flow.

The temporal evolution of zonally integrated meridional (both north- and southward) velocity anomalies along depth is shown in Fig. 3e–h — revealing a generalized slow-down of the AMOC upper limb from 2000s on, for all sections. Since at 6.5°S and 26.5°N the AMOC upper limb flow is concentrated within the western boundary NBUC and Gulf Stream, respectively, which have their cores lying in the upper ∼500 m (Fig. 3c, d), the decreasing anomalies are centered above this layer in both these sections (Fig. 3g, h) — whereas the 34°S and 24.5°S AMOC sections display widespread decreasing anomalies over the whole water column (Fig. 3e, f). This owns to three reasons: (i) the weakened northward AMOC upper limb flow is found spread across the basin interior at 34°S and 24.5°S, contributing to enhance negative anomalies along all depths; (ii) the strengthened southward BC is a deep current near 34°S (Fig. 3a)[124] — contributing to deepen negative anomalies; (iii) while near 24.5°S the BC is considered rather weak and shallow (Fig. 3b)[126], since it lies above the NBUC, which is shown to be weakening — so that a stronger shallow BC on top of a weakened deeper NBUC combine to produce vertically uniform negative anomalies.

In summary, at 34°S the deep negative anomalies are dominated by the intensification of a deep BC along its entire vertical extension (Fig. 3a, e); at 24.5°S the negative anomalies represent both the intensified shallow BC above ∼250 m and the generalized slow-down of the AMOC upper limb (which in this section flows both along the widespread northwestward BeC-sSEC system to the east and the narrow subsurface NBUC to the west, just off the western boundary) (Fig. 3b, f); while at 6.5°S and 26.5°N, shallower and intense negative anomalies are mostly associated with the decreased NBUC and Gulf Stream transports, which are the main conduits for the AMOC upper limb at these sections (Fig. 3c, g and d, h, respectively). A shoaling of the AMOC upper limb is also illustrated (gray contours in Fig. 3e–h) — its vertical extent shrinks below 1 km along 2000–2100 at all of the four sections, from 34°S to 26.5°N.

SASG structural changes. The altered transports of ocean currents generate shifts in flow distribution patterns, which in turn affect the three-dimensional structure of the subtropical gyre.

Flow redistributions. (i) An EOF analysis of zonal velocity anomalies illustrates how the circulation along the westward northern limb of the SASG is projected to change (Fig. 4a, b). The region where the mean flow is westward-oriented is delimited by the black thick contour, while the background shading represents
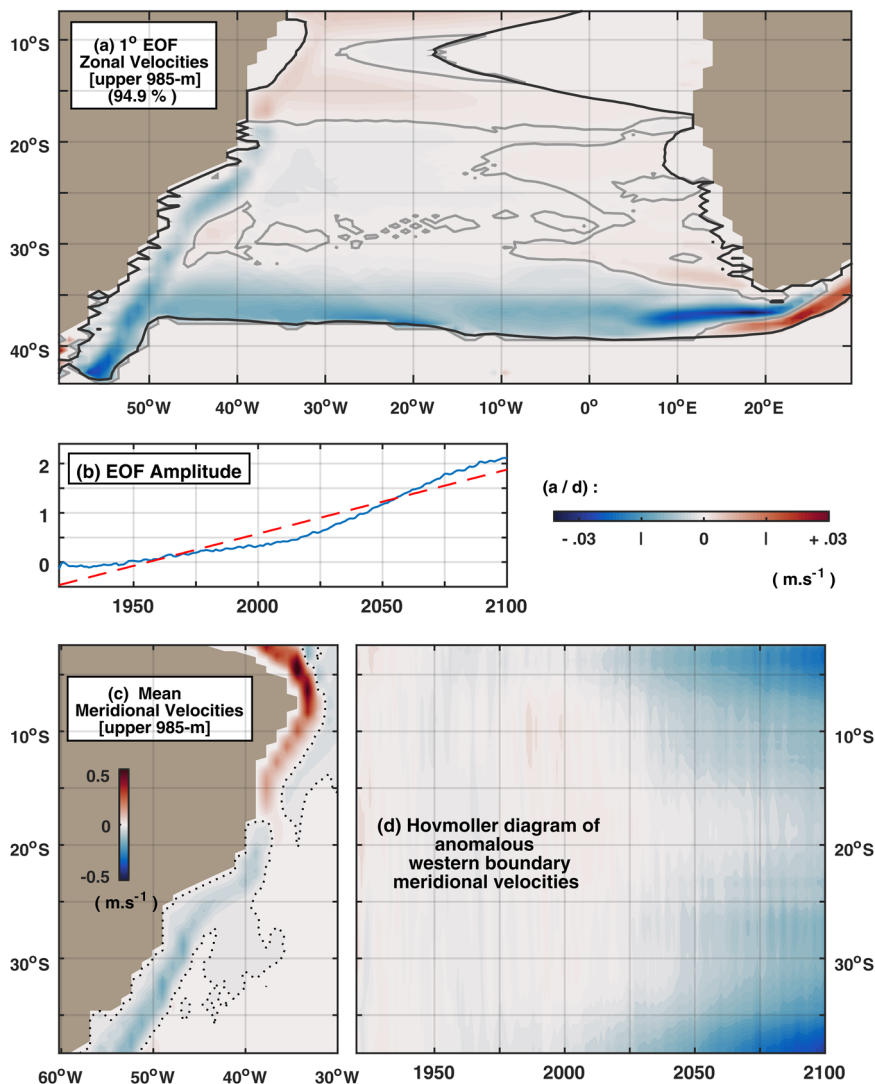
Fig. 4 Changes in the distribution of zonal and meridional SASG flows. a Spatial pattern of the leading EOF (94.9% of total variance) of zonal velocity anomalies along 1920–2100 within the upper 985-m of the South Atlantic subtropical gyre (delimited by the 1920–2100 mean zero zonal velocity line — black filled contour). Trends were not removed from the data prior to performing the EOF. **b** Corresponding dimensionless amplitude, or Principal Component (PC), time series (blue) and its linear trend along 1920–2100 (red dashed line). **c** 1920–2100 mean, upper 985-m, meridional velocities along the SA western boundary, showing the north-south distribution of the WBCs, for reference. **d** Hovmoller diagram of anomalous meridional velocities averaged over the western boundary layer (within a 6°-longitude band off the South American coast), corresponding to the meridional extension in **c**.

the anomalous zonal flows that are superposed on the mean circulation, as the spatial pattern of the leading EOF mode (Fig. 4a). The transit of waters crossing the SA basin from the eastern to the western boundary is accomplished by the BeC-sSEC system — the eastern and northern limbs of the SASG. However, considering that the gyre's shape in the horizontal plane is not circular, but instead depicts a D-like format[119], the BeC-sSEC system is actually northwestward oriented, and thus the eastern boundary BeC itself also has a strong westward component[120]. It is shown that, while westward velocities are reduced along the conventional BeC-northern sSEC route (outer portions of the eastern-to-northern boundaries marked with easterly anomalies in red), a westward strengthening occurs mainly from the AL region south of the African continent directly towards the southern sSEC, zonally crossing the basin interior and feeding the BC at its final portions (blue shading) — also as according to Figs. 1b, 2. The BC is represented by its westward component following the coastline orientation (Fig. 4a) and, as previously suggested, it strengthens since its origins because even

the central and northern portions of the sSEC are mostly bending southwards instead of northwards. The Agulhas system change pattern described in the previous section is also elucidated by this EOF spatial pattern, displaying a projected narrowing of the AL into the SA basin interior. These results are further discussed in terms of mechanisms in Section 2.4 and in comparison to previous studies in the SI, item 11.

(ii) Fig. 4c, d concern the north-south spreading of the waters brought by the AL-BeC-sSEC system across the South American coast, along the northward NBUC (red shading) and southward BC (blue shading): the development of southward anomalous flows is observed both to the north and south of the mean sSEC bifurcation region (Fig. 4d), further supporting the projected BC strengthening and NBUC/AMOC upper limb weakening. Diffuse and weak anomalies emerge from the 2000s on, confined to the northern- and southernmost ends of the NBUC and BC, respectively. After ~ 2050, the NBUC/BC anomalies spread meridionally, converging towards each other, indicating that the NBUC (BC) is projected to gradually weaken (strengthen)
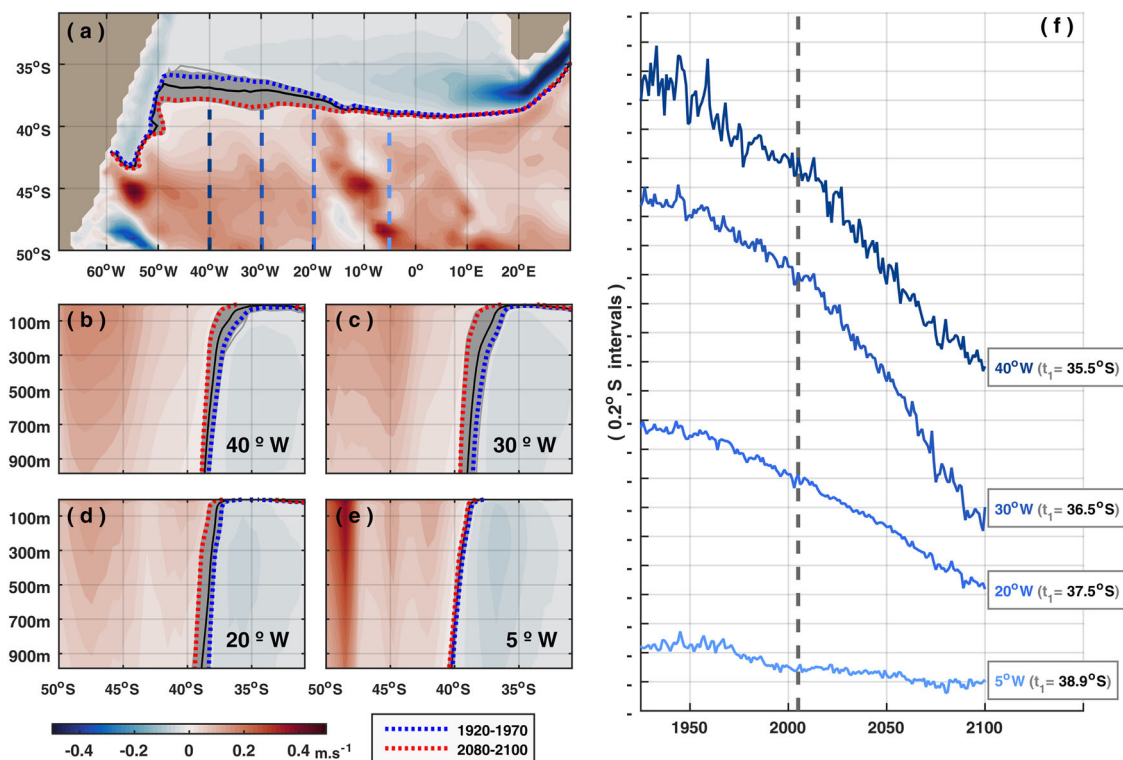
Fig. 5 Poleward shift of the western SASG center. 1920–2100 mean zonal velocities (background colors): (**a**) at the zonal-meridional plane, averaged over the upper 985-m; **b**–**e** and along depth at 40°W, 30°W, 20°W and 5°W, respectively. **a**–**e** The mean zero zonal velocity line is shown for: 1920–2100 (black filled contour), 1920–1970 (blue dotted contour) and 2080–2100 (red dotted contour); gray filled contours show its annual evolution along 1920–2100. Vertical dashed lines in **a** correspond to the locations where vertical profiles are shown in **b**–**e** as well as to where time series of the zero zonal velocity line were derived at 100-m depth – shown in **f**. The value corresponding to the first time step (1920) of each time series is indicated, while the y-axis varies in 0.2°-latitude intervals (increasing from south to north, thus sign convention is negative downwards for a southward migration of the zero zonal velocity line). The gray dashed vertical line indicates the transition from the historical (1920–2005) to the RCP8.5 (2006–2100) period.

across its whole extension, up to its site of origin, near the sSEC bifurcation region.

Resulting boundary displacements. (i) At the southwestern SA, the zero zonal velocity line between 30°–40°S (which marks the transition from sSEC westward flows to the north and SAC eastward flows to the south) is displaced southward from 1920–1970 to 2080–2100, along ~50°–15°W (Fig. 5). This meridional shift is slightly more pronounced at the upper layers (Fig. 5b, c), but it is also extended in depth (Fig. 5b–d). Dynamically, it can be interpreted in terms of a projected shift in the direction of the sSEC westward flow passing to the north: while it used to be more northwestward-oriented, as normally expected, it tends to follow a straighter zonal route towards the western boundary in the future, linking the AL directly to the southern termination of the BC (e.g., Figs. 1, 4a) and therefore pushing the southern limit of the sSEC to the south, west of the middle of the basin where the flow is diverted from its climatological position.

(ii) The SASG northernmost limit close to the western boundary, represented by the sSEC bifurcation latitude (SBL) (orange/black circle in Figs. 1a/2b), is projected to migrate northward instead, with a meridional shift that is conversely less (more) pronounced at upper (deeper) layers (Fig. 6), implying a less inclined bowl-shape — which is typical of wind-driven subtropical gyres, globally[127,128] — limiting the SASG to the north. The northward displacement of the SBL is in agreement with the BC strengthening and NBUC weakening[24,95,119] (e.g., Fig. 4d), and it corroborates that even though the northern sSEC does not decrease at a rate comparable to that of the NBUC, the westward sSEC flow is being unevenly distributed, favoring the

southward BC and therefore recirculating in the SASG — meaning that even central and northern portions of the sSEC which are generally prone to feed the northward NBUC-NBC system[24,129] (directly or indirectly by taking a tour along equatorial pathways) are actually being relocated to turn southward in their majority.

The NBUC is the main conduit for the AMOC upper limb downstream the sSEC bifurcation[24,28,29], and its lower base is also projected to get shallower, progressively from ~ 24°S to ~ 7°S (Fig. 6a), in accordance with the shallowing trend for the AMOC upper limb across all transbasin sections (Fig. 3e–h) based on the location of the maximum AMOC streamfunction[58].

The values associated with the northward migration of the SBL (Fig. 6) and the southward migration of the zero zonal velocity line at the southern limit of the sSEC (Fig. 5) are displayed in Supplementary Table 2.

(iii) However, at the SASG meridional center, to the east (30°–10°W), the sSEC system shifts southward entirely — at its southern as well as at its northern edge (Supplementary Fig. 5a), with the southward shift at the northern edge being larger at deeper layers, analogous to the northward shift of the SBL west of that (at the SASG northernmost boundary off the South American coast).

The mean vertical structure of the sSEC system (and consequently of the sSEC bifurcation as well) is depth dependent at its northern limit, i.e., it shifts poleward with increasing depth[24]. It is clearly shown that, far from the western boundary, the whole sSEC system is slowing down along outer, northern portions while speeding up along inner, southern portions (Supplementary Fig. 5c, d). This causes a poleward retraction of the sSEC system across the basin interior. Just off the western boundary, in turn, the SBL shifts
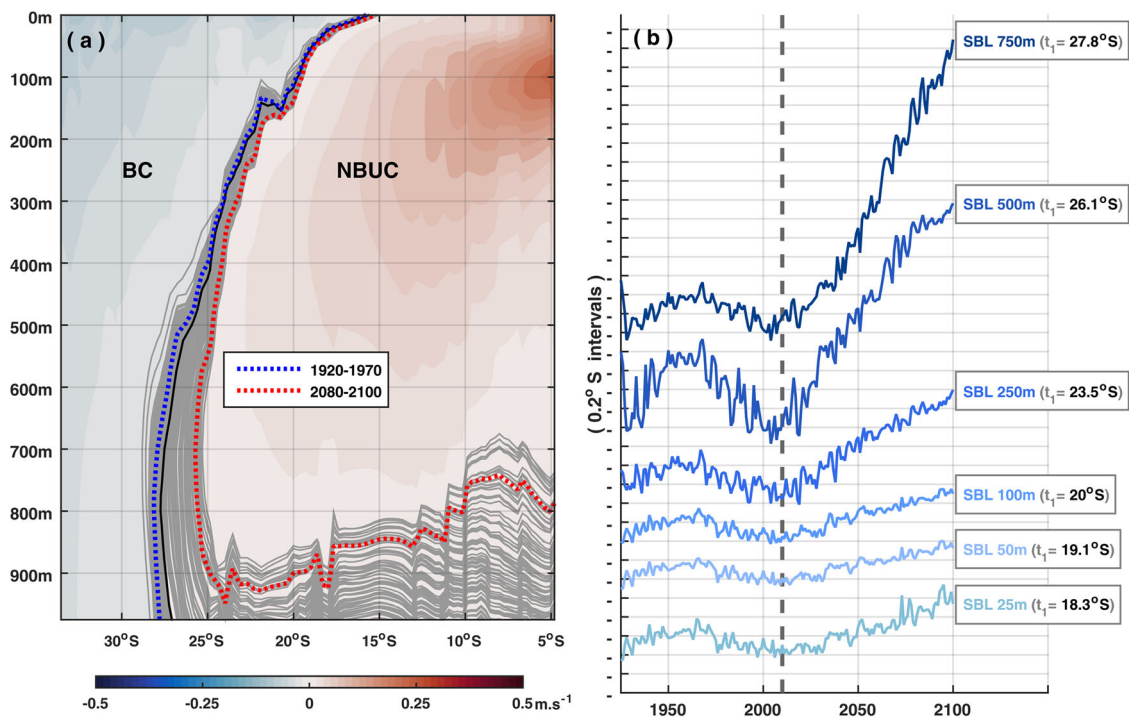
Fig. 6 Equatorward shift of the sSEC bifurcation latitude at the SASG northwestern boundary. a 1920–2100 mean meridional velocities averaged over the western boundary layer (<4° from the South American coast). Positive (negative) values indicate northward (southward) flows associated with the NBUC (BC). The bifurcation of the sSEC is represented by the zero meridional velocity line, shown for the mean periods of 1920–2100 (black filled contour), 1920–1970 (blue dotted contour) and 2080–2100 (red dotted contour); gray filled contours show its annual evolution along 1920–2100. **b** Time series of the sSEC bifurcation latitude at different depths. The value corresponding to the first time step (1920) of each time series is indicated, while the y-axis varies in 0.2°-latitude intervals (increasing from south to north, thus sign convention is positive upwards for a northward migration of the SBL). The gray dashed vertical line indicates the transition from the historical (1920–2005) to the RCP8.5 (2006–2100) period.

equatorward in response to the increased (decreased) BC (NBUC) transport, as expected[24,95,119].

A more comprehensive description of the SASG structural changes and associated mechanisms is provided in the SI, items 6-7. Essentially, the SASG is distorted from its mean state. At the western portion, its northern boundary is projected to expand meridionally: with the SBL shifting northward at deeper layers (Fig. 6) and the southern base of the sSEC shifting southward, conversely with a larger shift at upper layers (Fig. 5). While, far from the western boundary to the east, between 30°–10°W, the whole sSEC system flowing along the northern boundary shifts southward, with the shift at the northern limit being greater in deeper layers. In other words, the SASG northern limb is projected to change its structure non-homogeneously across the horizontal-depth plane — characterizing a vertically tilted meridional expansion of its western portion and a nearly-systematic southward drift of its central portion.

Mechanisms and discussion. The wind stress is a driving agent of ocean currents, but it is its horizontal gradient rather than its absolute strength that mostly matters — the large-scale wind stress curl (WSC), which is in general the major forcing mechanism of the upper ocean[130]. Changes in the local basin-scale wind-driven circulation can also be plausibly inferred from changes in the Sverdrup transport field[131], which yields a relation for wind-forced flow transport dominated by the Earth's rotation. In summary, anticyclonic WSC provides the torque that drives the circulation of global subtropical gyres, resulting in equatorward Sverdrup transport in the interior of each ocean basin, compensated by a strong poleward current at the western boundary[132]. This combination causes the flow to converge in the center of subtropical gyres, which are characterized by higher sea

surface height (SSH) values than at the edges[133,134]. Therefore, low-frequency surface wind stress variations force upper-ocean water mass redistributions which are in turn reflected in SSH spatial changes. To explore the mechanism behind the ocean circulation changes presented here, we have investigated concurrent changes in the wind pattern (horizontal wind stress, wind stress curl and Sverdrup transport) and the SSH field (Supplementary Figs. 6–8).

The trends along 1920–2100 of the wind stress (superposing vectors) and WSC (background shading) anomalies are shown in Supplementary Fig. 6b, where the black contour represents the climatological zero WSC line, which limits the positive curl governing southern subtropical gyres and allowing their pan-Southern Ocean connectivity to the south[79]. The horizontal wind stress drives a cyclonic (negative, blue) WSC anomaly over most of the SASG (north of ~45°S), which may seem counter-intuitive to our results at first, but it is in fact consistent with the weakening of the anticyclonic SASG loop along its northernmost boundary (e.g., Figs. 1/S6a, 4a, S5d), as well as with the decreased northward transport along the AMOC upper limb — since these anomalous winds tend to hinder the arrival of sSEC waters at the western boundary to feed the NBUC/NBC system. Moreover, anomalous zonal winds blowing from the Indian Ocean into the SA up to the western boundary are in agreement with the intensified westward AL-southern sSEC route (Figs. 1, 2 — time series 12-13, 4), once climatological westerlies and their associated northward Ekman transport are weakened, thus hampering the climatological north-westward AL route into the SA and instead favoring a straighter westward route.

In turn, at the western portion of the basin (west of 20°W, between ~ 25°–50°S), the presence of persistent easterly wind stress

anomalies suggests that these act to push the sSEC flow towards the southwestern SASG boundary, thus contributing to strengthening the BC and the SAC (Figs. 1b, 2 — time series 10/14 and 11). Even though these anomalous easterlies blow against the SAC flow around 45°S, their associated anomalous southward Ekman transport causes waters to converge over the SAC; beyond that, mass conservation is satisfied: as the strengthened BC meets with a likewise strengthened MC at the BMC region (Figs. 1, 2), by continuity a stronger eastward SAC is formed at the SASG southern boundary. The SAC strengthens up to ~20°W (Supplementary Fig. 6a); downstream of that, the wind anomalies indeed seem to induce its flow to either recirculate in the SASG via intra-gyre pathways[12,122] or join the ACC along higher latitudes[118].

At the broad scale, the weakened westerlies (i.e., easterly anomalies) at subtropical latitudes (around 45°S) and strengthened westerlies over the circumpolar region (around 60°S) are associated with a positive phase of the Southern Annular Mode (SAM—the leading mode of SH extratropical atmospheric variability), which has experienced an increasingly positive trend since at least the second half of the 20th century, primarily in response to external forcing (ozone depletion and increasing CO_2)[135]. This anomalous wind pattern results in convergence (divergence) of the surface transport at the subtropics (near Antarctica), by increased southward (northward) Ekman transport, thus leading to an accelerated ACC (Supplementary Figs. 2–4)[63,136,137] and possibly also contributing to the increased SAC flow north of that. However, it has been demonstrated that the ACC response to these climate trends varies considerably across models, with some even predicting a reduction in its transport, owing to the influence of competing processes[138].

Also in association with the positive SAM trend, the meridional band between ~45°–60°S is dominated by positive WSC anomalies all the way from the Pacific to the Indian sector, suggesting a southward shifting, intensifying circulation at the southern edge of the SHSG, as postulated in previous studies[79–81,92,93]. This also implies a strengthened interbasin connectivity of the supergyre[79], favoring flow exchanges[93] as through the AL[105] and the DP — which are shown to increase their transports into the SA (Figs. 1, 2 — time series 5/6, 12).

Accordingly, the Sverdrup balance implies an intensification of the SASG basin interior transport at its southern portion along with a poleward expansion of the gyre over the whole zonal extension of the basin (Supplementary Fig. 5c, indicated by the zero zonally integrated WSC line over 1920–1970 versus 2080–2100). More specifically, the SASG interior is projected to spin-down between ~15°–45°S and to spin-up south of that, as a result of the local WSC anomalies. Though note that Sverdrup dynamics prevail only far from the western boundary[139], and therefore do not directly illustrate the strengthening of the BC (happening from 20°S downstream); which is, according to this theory, indirectly represented by the compensating northward transport in the basin interior.

However, the degree to which the real SASG interior transport is in Sverdrup balance might be compromised by density-driven changes in the AMOC and by the inflow of interocean waters with distinct physical properties. Overturning and gyre circulations are fundamentally linked[140], and the SA is especially sensitive to both low-frequency buoyancy-forced variations due to perturbed AMOC dynamics and wind-forced changes[102]. It is far out of our scope to categorically investigate the reasons for a projected AMOC slow-down, still, changes in high-latitude AMOC forcing are expected to call for compensating effects involving upstream surface AMOC pathways[28–30]. As the AMOC weakens, it changes the meridional transport along the whole extension of the AMOC upper limb, including the subtropical oceans — hence potentially compromising the extent to which

the wind field determines the flow in the ocean interior[141]. And this is particularly meaningful for the SA — where the AMOC upper limb travels precisely along the subtropical gyre interior, which is the target region described by the Sverdrup theory. Therefore, interbasin transfers[142] and flow compensations as adjustments to changes in overturning might partially offset the changes induced by the shifted wind pattern via Sverdrup dynamics.

Moreover, the climatological wind-driven BC is known to be weak among global WBCs, since the larger portion of the sSEC normally forms the NBUC along the AMOC upper limb[129,143]. In a warming climate with a declining AMOC, the opposite holds true: as the NBUC weakens, the sSEC then feeds the BC to a larger extent. Since the mean BC transport is not well explained only by surface wind variations, the same is expected for changes in its projected transport[98].

As described throughout this section, it is found a good correspondence between changes in the general circulation (depicted by the horizontal velocity field) and wind field changes, but the response of SA ocean currents to wind-forcing is better understood through a large-scale, continuity perspective — since change patterns are not exactly mirrored and the Sverdrup dynamics is not the only one at play. Overall, the WSC and Sverdrup transport change patterns are consistent with the notion of a southwestward strengthening of the SASG (Supplementary Fig. 6), where the positive anomalies of the WSC and of the horizontal velocities' absolute magnitude are correlated at $r = 0.52$ (Supplementary Fig. 6d).

Finally, as wind anomalies act to pile up waters at the western and southern portions of the SASG, the sea level tends to rise over these regions (Supplementary Fig. 7). That is because spatially varying SSH trends reflect the geographical redistribution of upper-ocean water masses[68,70,92,144–146]. In the mean climatology (Supplementary Fig. 8), wind-driven convergence forms a SSH hill at the SASG center, with its anticyclonic geostrophic circulation revolving around a maximum SSH. Under future climate change, the SASG center is displaced poleward, while the sea level tends to drop over its weakened northern boundary.

Around the southern boundary, the strong positive SSH signal extending west of 20°W towards the Indian basin is another fingerprint of the positive SAM trend, resulting from a broad-scale anomalous Ekman convergence (Supplementary Fig. 6b). It has been demonstrated in accordance with our results that while over SH high latitudes the sea level rise is below the global average trend, over SH midlatitudes enhanced regional sea level rise prevails, reflecting the southward migration of southern subtropical gyres[92]. This anomalous SSH pattern also agrees with the enhanced ACC transport over these regions (Supplementary Figs. 3–4).

Conclusions
We have described a projected scenario of externally-forced changes in the SA upper-ocean circulation, involving the interplay between AMOC upper limb and SASG pathways. The CESM1-LE simulates an AMOC decline over the 21st century, which is in line with the prediction of most last-generation CMIP5 and CMIP6 models[58,147,148]. While the majority of efforts to understand the AMOC dynamics and variability are still focused on the North Atlantic, our results provide modeling evidence for upstream circulation changes, taking place in the SA basin — where the AMOC upper limb is primarily originated through the incorporation of interocean waters into the SASG circulation.

Our results suggest that even though Pacific and Indian contributions to form the AMOC upper limb are projected to actually increase instead of decrease in the future, the bulk of these cold- and warm water routes are either lost to the ACC system continuing

eastward to exit the SA basin, or directed to recirculate into a deformed SASG — which displays a spun-up southwestern core (BeC-central/southern sSEC-BC-SAC) in contrast with a weak circulation at its northern boundary (northern sSEC) that translates into a pronounced decline in strength of the northward AMOC upper limb (through the NBUC-NBC system, primarily). The SASG spatial structure is also projected to change non-homogeneously across the horizontal-depth plane, in response to the altered transport of its boundary currents.

Predicted surface wind stress changes lie behind these modified upper-ocean flows. The anticyclonic WSC which provides the torque to drive the subtropical gyre circulation is shown to weaken over the northern areas of the SASG where transports are decreased. From the Indian Ocean towards the SA western boundary, anomalous easterlies induce an increase in the Agulhas leakage and its westward extension across inner portions of the northern boundary sSEC, converging waters towards the BC and the SAC at the western and southern boundaries of the SASG — hence its southwestern spin-up.

Moreover, broad-scale wind and sea surface height anomalies indicate that anthropogenic SH climate trends may persist into the future — with the upward SAM trend driving a poleward shift and an enhanced circulation at the southern edge of the SH oceanic supergyre.

Essentially, our main conclusion is that: once in the subtropical SA, most of the source waters that are supposed to compose the upper limb of the AMOC (from the Pacific, Indian and SA interior) are not reaching their destination; instead, these waters are being diverted from the AMOC upper limb route by approaching the western boundary to recirculate in the SASG. Thus, relying on the principle of mass conservation: since more interocean waters are being incorporated into SA subtropical waters along their anticyclonic loop, it is concluded that the reduction of waters escaping the subtropical gyre to the north and proceeding along the AMOC upper limb is being compensated by an increase in the amount of waters that remain in the gyre's loop — by initially bending southward along the western boundary BC. In other words, a weakened AMOC upper limb is compensated by a strengthened SASG circulation, according to CESM1-LE simulations.

More specifically, with focus on the SA sector, our main findings can be outlined as follows:

1. Projected SASG circulation changes are asymmetrically distributed, presumably under the influence of combined wind and buoyancy forcings;
2. Warming-induced shifted atmospheric patterns translate into a strengthened SASG interior transport at its southern domain, based on the Sverdrup balance;
3. However, superimposed on the surface wind forcing, is a declining transport throughout the interhemispheric AMOC upper limb spanning the Atlantic basin from south to north—which might be attributed to many factors that are out of our scope, such as changes in high-latitude deep water formation;
4. Also due to the weakened AMOC upper limb, the sSEC tends to recirculate in the SASG rather than extending into the equator, thus further strengthening the BC transport — beyond of what is predicted based solely on the Sverdrup dynamics (which indirectly infers the BC transport through its compensating basin interior flow of opposite direction);
5. The interplay between wind and buoyancy systems results in our main conclusion: within the SA basin, a weakened AMOC upper limb is compensated by a strengthened SASG circulation as according to our simulation results.

6. Lastly, the SASG three-dimensional configuration changes in adjustment to wind- and buoyancy-driven flow redistributions — with meridional shifts that are larger in deeper (upper) layers being associated with buoyancy-forced (wind-forced) fluxes. In general, off the South American coast the SASG northern boundary (depicted by the SBL) shifts northward at deeper layers in response to the AMOC decline; while at eastern portions the whole sSEC system at the northern boundary shrinks southward due both to the weakened circulation along the northern SASG inferred from cyclonic WSC anomalies and to the AMOC decline. In the meridional interior of the basin, the boundary between westward and eastward flows is displaced southward at western domains in response to surface wind anomalies. At the southern boundary, the SASG is entirely displaced poleward according to wind-related and SSH fields, following hemispheric-scale atmospheric trends. Together, these shifts act to reshape the SASG spatial configuration, giving rise to a deformed SASG — which is extremely different from the mean climatological one.

It is not clear through our results the degree to which wind-driven subtropical circulation changes may influence the AMOC slow-down, and vice-versa. Our intention was to describe the long-term response of SA dynamics to these concomitant changes. We believe both the increasing SAM trend and the density-driven reduction of the AMOC strength might work in synergy to produce the simulated scenario that is here illustrated.

In any case, intrinsic South Atlantic circulation processes can determine whether interocean fluxes of heat and freshwater are transported northwards eventually affecting AMOC deep convection or not[16,77,149]. In this context, the wind forcing seems to play a key role[17,20,150], by affecting the strength and orientation of ocean currents and thus the horizontal and vertical transports of heat and salt[105,151–155] — therefore modifying basin-scale gradients of pressure and meridional density which are critical in setting the overturning strength[114,156,157].

The CESM-LE ensemble mean here employed effectively cancels out unforced internal climate variability, resulting in changes only due to external forcings. In view of that, our results point to a major reorganization of SA ocean dynamics, essentially as a consequence of rising greenhouse gases (the dominant factor among external forcings) — suggesting that human activity is rapidly reshaping Earth's climate[158].

As anthropogenic global warming continues, the ocean surface temperature response is modulated by changes in large-scale atmospheric and oceanic circulation dynamics — such as a weakening AMOC and altered patterns of gyre-scale variability.

The AMOC upper limb and the SASG are components of the GOC, which can be basically defined as the global-scale motion of the ocean that includes wind- and buoyancy-driven fluxes linking upper and deeper layers to circulate and redistribute fundamental properties around the globe. Among these properties, are heat and carbon (as CO_2) — the main products of human activities. As excess heat and CO_2 in the atmosphere are uptaken by the ocean[159,160] through mechanisms that are part of the GOC[161–166], ocean circulation changes influence the rates and patterns of heat/carbon uptake and storage[167–169], thus compromising the mitigation of atmospheric warming[170] on the one hand, and further leading to adverse regional effects such as thermal expansion causing sea level rise, and ocean acidification[171] on the other hand. Specific implications of AMOC upper limb and SASG changes are discussed in the SI, item 12.

This study complements important pieces of information with respect to the recent literature reporting current and future ocean circulation changes in response to anthropogenic climate change.

Up to now, no study has approached long-term projected changes in SA upper-ocean circulations considering the interplay between the AMOC upper limb and the SASG, let alone from the perspective of single-model large ensemble simulations. Our results are in fair agreement with several other simulation and observational results recently reported in the literature, which are listed and discussed in the SI, item 11. Nonetheless, the results here presented should be interpreted with due caution, as they are limited by the fidelity of the model employed. Studies using independent models as well as observation-based and proxy data are highly desirable for confirming our findings.

Methods

The Community Earth System Model Large Ensemble project. The numerical results of the National Center for Atmospheric Research (NCAR) Community Earth System Model (version 1) Large Ensemble Project (CESM1-LE) are used[106]. The CESM1-LE represents a community resource for studying climate change in the presence of internal climate variability. It includes a 40-member ensemble of fully-coupled CESM1 simulations for the period of 1920–2100. Each member is subject to the same radiative forcing scenario (historical up to 2005 and RCP8.5 thereafter), but begins from a slightly different initial atmospheric state (created by randomly perturbing temperatures at the level of round-off error).

All the simulations are derived from the CMIP5 version of the CESM[172]. The horizontal resolution is at ~1° in all model components. The experiment includes a multi-century control integration followed by a transient integration (ensemble member 1) which started at year 402 of the control and was integrated for 251 years under historical forcing (1850–2005). Next, the protocol for running projections in CMIP5 models is applied. The projection scenario used in these runs was established by the IPCC, and is referred to as the RCP8.5 scenario, for 2006–2100. The additional ensemble members were initialized from ensemble member 1 at January 1920 with the round-off level perturbations applied to the air temperature field.

To make meaningful interpretations about past to future SA overturning circulation trends, a deeper understanding of the competing roles of natural climatic variability and forced change is required. Since different models have different sensitivities to an identical set of radiative forcings[173,174], they end up generating exclusive sequences of internal variability — making this inherent uncertainty undersampled by multimodel ensembles. Here, the use of a single-model large ensemble eliminates structural differences inherent to multi-model ensembles, allowing the spread across the ensemble to be entirely attributed to the internal variability of the modeled climate system.

For each ensemble member, temporal trends in any variable can be separated into two parts: (1) the forced trend that is common across all ensemble members, and (2) the unforced, or internal trend, that occurs only in that ensemble member. The ensemble mean averages out natural intrinsic climate variability and thus represents the forced response — which is dominated by anthropogenically forced climate change.

The results shown here represent the ensemble mean of the 40-full-forcing members for the historical period (1920–2005, 20TR) and future climate change projections (2006–2100, RCP8.5).

Data analysis. Prior to averaging CESM1-LE members, annual means were obtained from the original monthly mean data set in order to remove higher-frequency variability which we are not particularly interested in. Since the focus of this study is on the upper-ocean pathways of SA circulations, nearly all analysis concern the upper 985-m depth, using the original model depth levels for vertical integrations. Vertical profiles are shown up to 3–5 km for reference.

The volume transports time series were obtained by horizontally and vertically integrating the zonal (u) or meridional (v) velocities along model grid cells. When calculating positive (negative) velocities, i.e. northward or eastward (southward or westward), only positive (negative) values are considered, in order to avoid adjacent counterflow interference, with the exception of MOC streamfunction time series (Fig. 2, time series 21b-24b). Transport time series are derived for individual zonal/meridional coordinates (transects) or for zonal/meridional ranges (boxes); in the latter case, the transport time series corresponding to each coordinate within the selected range was first obtained, then these individual time series were averaged to represent the mean transport across a wider range only if they were considered to have very similar low-frequency variability and, mainly, long-term trends. Thus, the transport time series corresponding to a particular box expresses low-frequency signals and changes that are common to all transects which compose that respective box, for simplification. In other words, boxes are used to show that the transport of ocean currents is changing consistently across those regions, signalizing the spatial magnitude of changes.

The numbering scheme in Fig. 2 was designed to best match the description of up- to downstream flow changes in Section 2.2. In a few cases, the sequence had to be adjusted in order to accommodate the time series in Fig. 2c–e.

All volume transports are vertically integrated up to 985-m, with the exception of MOC streamfunction time series, which are vertically integrated up to the lower limit of the northward AMOC upper limb in each time step (i.e., up to the depth of transition between northward and southward velocities). The absolute magnitude of the horizontal velocities is defined by $\sqrt{u^2 + v^2}$, applied to each grid point of the domain.

Anomalies are derived with respect to the 1920–1970 base period, corresponding to the first 50 years of the historical period (20TR) when climate change signals were relatively modest. Zonal-meridional maps and meridional-depth profiles of trends correspond to the total trend with respect to 1920–2100. 1920–1970/2080–2100 differences are shown, aiming at demonstrating the contrast between a period before greenhouse gas emissions became to increase exponentially and a projected period in the late 21st century which reflects the future changes expressed by the high-end RCP8.5 scenario.

For the Empirical Orthogonal Function (EOF) analysis (Fig. 4a, b), anomalies with respect to the 1920–1970 base period are used. The EOF analysis is used to extract the dominant pattern of variability in the zonal flow field of the SASG under external forcing. Intentionally, the data was not detrended prior to performing this EOF, in order to evidence the anthropogenically-forced signal in the time series. Generally, linear detrending is supposed to remove externally-forced signals, leaving the signature of potential modes of internal climate variability. However, internal variability is already averaged out when performing the CESM-LE ensemble mean. Removing the linear trends from each grid point prior to performing the EOF analysis results in a nearly identical EOF spatial pattern. Therefore, focus is given to the interpretation of this spatial pattern in terms of its dynamical implications, as anthropogenic forcing acts to reinforce this pattern into the future.

Statistical significance of long-term trends was estimated with the non-parametric Mann-Kendall test[175,176]. The linear relations between time series (Figs. S2–S4) were quantified using Pearson's correlation coefficient[177]. All the correlations shown are statistically significant at the 99% confidence level, inferred from a t-test.

Data availability

The CESM1-LE data set used in this study can be directly accessed through https://www.earthsystemgrid.org/dataset/ucar.cgd.ccsm4.cesmLE.html.

Code availability

The data analyses and figures presented in this article were conducted using MATLAB_R2021b. Codes are available upon request by contacting the corresponding author.

References

1. Buckley, M. W. & Marshall, J. Observations, inferences, and mechanisms of the Atlantic Meridional Overturning Circulation: a review. *Rev. Geophys.* **54**, 5–63 (2016).
2. Bower, A. et al. Lagrangian views of the pathways of the Atlantic Meridional Overturning Circulation. *J. Geophy. Res.: Oceans* **124**, 5313–5335 (2019).
3. Talley, L. D. Closure of the global overturning circulation through the Indian, Pacific, and Southern Oceans: schematics and transports. *Oceanography* **26**, 80–97 (2013).
4. Cessi, P. The global overturning circulation. *Ann. Rev. Marine Sci.* **11**, 249–270 (2019).
5. Gordon, A. L. Indian-Atlantic transfer of thermocline water at the Agulhas retroflection. *Science* **227**, 1030–1033 (1985).
6. Gordon, A. L. Interocean exchange of thermocline water. *J. Geophys. Res. Oceans* **91**, 5037–5046 (1986).
7. Rühs, S., Durgadoo, J. V., Behrens, E. & Biastoch, A. Advective timescales and pathways of Agulhas leakage. *Geophys. Res. Lett.* **40**, 3997–4000 (2013).
8. Rintoul, S. R. South Atlantic interbasin exchange. *J. Geophys. Res.: Oceans* **96**, 2675–2692 (1991).
9. Friocourt, Y., Drijfhout, S., Blanke, B. & Speich, S. Water mass export from Drake Passage to the Atlantic, Indian, and Pacific oceans: a Lagrangian model analysis. *J. Phys. Oceanogr.* **35**, 1206–1222 (2005).
10. Speich, S., Blanke, B. & Madec, G. Warm and cold water routes of an OGCM thermohaline conveyor belt. *Geophys. Res. Lett.* **28**, 311–314 (2001).
11. Rühs, S., Schwarzkopf, F. U., Speich, S. & Biastoch, A. Cold vs. warm water route–sources for the upper limb of the Atlantic Meridional Overturning circulation revisited in a high-resolution ocean model. *Ocean Sci.* **15**, 489–512 (2019).

12. Drouin, K. L. & Lozier, M. S. The surface pathways of the South Atlantic: revisiting the cold and warm water routes using observational data. *J. Geophys. Res.: Oceans* **124**, 7082–7103 (2019).

13. Wood, R. A., Rodríguez, J. M., Smith, R. S., Jackson, L. C. & Hawkins, E. Observable, low-order dynamical controls on thresholds of the Atlantic Meridional Overturning Circulation. *Clim. Dyn.* **53**, 6815–6834 (2019).

14. Evans, D. G. et al. Recent wind-driven variability in Atlantic water mass distribution and meridional overturning circulation. *J. Phys. Oceanogr.* **47**, 633–647 (2017).

15. Jamet, Q. et al. Locally and remotely forced subtropical AMOC variability: a matter of time scales. *J. Clim.* **33**, 5155–5172 (2020).

16. Garzoli, S. & Matano, R. The South Atlantic and the Atlantic meridional overturning circulation. *Deep Sea Res. Part II Top. Stud. Oceanogr.* **58**, 1837–1847 (2011).

17. Biastoch, A., Böning, C. W., Getzlaff, J., Molines, J.-M. & Madec, G. Causes of interannual–decadal variability in the meridional overturning circulation of the midlatitude North Atlantic Ocean. *J. Clim.* **21**, 6599–6615 (2008).

18. Biastoch, A., Böning, C. W. & Lutjeharms, J. Agulhas leakage dynamics affects decadal variability in Atlantic overturning circulation. *Nature* **456**, 489–492 (2008).

19. Leroux, S. et al. Intrinsic and atmospherically forced variability of the AMOC: Insights from a large-ensemble ocean hindcast. *J. Clim.* **31**, 1183–1203 (2018).

20. Speich, S., Blanke, B. & Cai, W. Atlantic meridional overturning circulation and the Southern Hemisphere supergyre. *Geophys. Res. Lett.* **34**, 1–5 (2007).

21. Van Aken, H. M. *The Oceanic Thermohaline Circulation: An Introduction* Vol. 39 (Springer Science & Business Media, 2007).

22. Stramma, L. & England, M. On the water masses and mean circulation of the South Atlantic Ocean. *J. Geophys. Res.: Oceans* **104**, 20863–20883 (1999).

23. Rousselet, L., Cessi, P. & Forget, G. Routes of the upper branch of the Atlantic Meridional Overturning Circulation according to an ocean state estimate. *Geophys. Res. Lett.* **47**, e2020GL089137 (2020).

24. Rodrigues, R. R., Rothstein, L. M. & Wimbush, M. Seasonal variability of the South Equatorial Current bifurcation in the Atlantic Ocean: a numerical study. *J. Phys. Oceanogr.* **37**, 16–30 (2007).

25. Talley, L. D. Shallow, intermediate, and deep overturning components of the Global heat budget. *J. Phys. Oceanogr.* **33**, 530–560 (2003).

26. Ganachaud, A. Large-scale mass transports, water mass formation, and diffusivities estimated from World Ocean Circulation Experiment (WOCE) hydrographic data. *J. Geophys. Res.: Oceans* https://doi.org/10.1029/2002JC001565 (2003).

27. Lumpkin, R. & Speer, K. Large-scale vertical and horizontal circulation in the North Atlantic ocean. *J. Phys. Oceanogr.* **33**, 1902–1920 (2003).

28. Zhang, D., Msadek, R., McPhaden, M. J. & Delworth, T. Multidecadal variability of the North Brazil Current and its connection to the Atlantic meridional overturning circulation. *J. Geophys. Res.: Oceans* https://doi.org/10.1029/2010JC006812 (2011).

29. Rühs, S., Getzlaff, K., Durgadoo, J. V., Biastoch, A. & Böning, C. W. On the suitability of North Brazil Current transport estimates for monitoring basin-scale AMOC changes. *Geophys. Res. Lett.* **42**, 8072–8080 (2015).

30. Tuchen, F. P., Brandt, P., Lübbecke, J. F. & Hummels, R. Transports and pathways of the tropical AMOC return flow from Argo data and shipboard velocity measurements. *J. Geophys. Res.: Oceans* **127**, e2021JC018115 (2022).

31. Rahmstorf, S. The thermohaline ocean circulation: a system with dangerous thresholds? *Clim. Change* **46**, 247 (2000).

32. Collins, M. et al. in *Climate Change 2013-The Physical Science Basis: Contribution of Working Group I to the Fifth Assessment Report of the Intergovernmental Panel on Climate Change*, 1029–1136 (Cambridge University Press, 2013).

33. Smeed, D. A. et al. Observed decline of the Atlantic meridional overturning circulation 2004–2012. *Ocean Sci.* **10**, 29–38 (2014).

34. Roberts, C., Jackson, L. & McNeall, D. Is the 2004–2012 reduction of the Atlantic meridional overturning circulation significant? *Geophys. Res. Lett.* **41**, 3204–3210 (2014).

35. Srokosz, M. & Bryden, H. Observing the Atlantic Meridional Overturning Circulation yields a decade of inevitable surprises. *Science* **348**, 1255575 (2015).

36. Rahmstorf, S. et al. Exceptional twentieth-century slowdown in Atlantic Ocean overturning circulation. *Nat. Clim. Change* **5**, 475–480 (2015).

37. Zhu, J., Liu, Z., Zhang, J. & Liu, W. AMOC response to global warming: dependence on the background climate and response timescale. *Clim. Dyn.* **44**, 3449–3468 (2015).

38. Jackson, L. C., Peterson, K. A., Roberts, C. D. & Wood, R. A. Recent slowing of Atlantic overturning circulation as a recovery from earlier strengthening. *Nat. Geosci.* **9**, 518–522 (2016).

39. Jackson, L. & Wood, R. Hysteresis and resilience of the AMOC in an eddy-permitting GCM. *Geophys. Res. Lett.* **45**, 8547–8556 (2018).

40. Smeed, D. et al. The North Atlantic Ocean is in a state of reduced overturning. *Geophys. Res. Lett.* **45**, 1527–1533 (2018).

41. Caesar, L., Rahmstorf, S., Robinson, A., Feulner, G. & Saba, V. Observed fingerprint of a weakening Atlantic Ocean overturning circulation. *Nature* **556**, 191 (2018).

42. Thornalley, D. J. et al. Anomalously weak Labrador Sea convection and Atlantic overturning during the past 150 years. *Nature* **556**, 227–230 (2018).

43. Weijer, W. et al. Stability of the Atlantic meridional overturning circulation: a review and synthesis. *J. Geophys. Res.: Oceans* **124**, 5336–5375 (2019).

44. Moat, B. I. et al. Pending recovery in the strength of the meridional overturning circulation at 26° N. *Ocean Sci.* **16**, 863–874 (2020).

45. Srokosz, M., Danabasoglu, G. & Patterson, M. Atlantic meridional overturning circulation: reviews of observational and modeling advances-an introduction. *J. Geophys. Res.: Oceans* **126**, e2020JC016745 (2021).

46. Li, H., Fedorov, A. & Liu, W. AMOC stability and diverging response to Arctic sea ice decline in two climate models. *J. Clim.* **34**, 5443–5460 (2021).

47. Worthington, E. L. et al. A 30-year reconstruction of the Atlantic meridional overturning circulation shows no decline. *Ocean Sci.* **17**, 285–299 (2021).

48. Caesar, L., McCarthy, G., Thornalley, D., Cahill, N. & Rahmstorf, S. Current Atlantic meridional overturning circulation weakest in last millennium. *Nat. Geosci.* **14**, 118–120 (2021).

49. Boers, N. Observation-based early-warning signals for a collapse of the Atlantic Meridional Overturning Circulation. *Nat. Clim. Change* **11**, 680–688 (2021).

50. Lohmann, J. & Ditlevsen, P. D. Risk of tipping the overturning circulation due to increasing rates of ice melt. *Proc. Natl Acad. Sci. USA* **118**, e2017989118 (2021).

51. MassonDelmotte, V. et al. In *Climate Change 2021: The Physical Science Basis. Contribution of Working Group I to the Sixth Assessment Report of the Intergovernmental Panel on Climate Change* (Cambridge University Press, 2021).

52. Gulev, S. K. et al. In *Climate Change 2021: The Physical Science Basis. Contribution of Working Group I to the Sixth Assessment Report of the Intergovernmental Panel on Climate Change* (Cambridge University Press, 2021).

53. He, F. & Clark, P. U. Freshwater forcing of the Atlantic Meridional Overturning Circulation revisited. *Nat. Clim. Change* **12**, 1–6 (2022).

54. Kilbourne, K. H. et al. Atlantic circulation change still uncertain. *Nat. Geosci.* **15**, 168–170 (2022).

55. Caesar, L., McCarthy, G. D., Thornalley, D. J., Cahill, N. & Rahmstorf, S. Reply to: Atlantic circulation change still uncertain. *Nat. Geosci.* **15**, 168–170 (2022).

56. Pörtner, H.-O. et al. *IPCC Special Report on the Ocean and Cryosphere in a Changing Climate* (IPCC, 2019).

57. Fox-Kemper, B. et al. In *Climate Change 2021: The Physical Science Basis. Contribution of Working Group I to the Sixth Assessment Report of the Intergovernmental Panel on Climate Change* (Cambridge University Press, 2021).

58. Weijer, W., Cheng, W., Garuba, O. A., Hu, A. & Nadiga, B. CMIP6 models predict significant 21st century decline of the Atlantic Meridional Overturning Circulation. *Geophys. Res. Lett.* **47**, e2019GL086075 (2020).

59. Swart, N. & Fyfe, J. C. Observed and simulated changes in the Southern Hemisphere surface westerly wind-stress. *Geophys. Res. Lett.* https://doi.org/10.1029/2012GL052810 (2012).

60. Kushner, P. J., Held, I. M. & Delworth, T. L. Southern Hemisphere atmospheric circulation response to global warming. *J. Clim.* **14**, 2238–2249 (2001).

61. Thompson, D. W. & Solomon, S. Interpretation of recent Southern Hemisphere climate change. *Science* **296**, 895–899 (2002).

62. Shindell, D. T. & Schmidt, G. A. Southern Hemisphere climate response to ozone changes and greenhouse gas increases. *Geophys. Res. Lett.* https://doi.org/10.1029/2004GL020724 (2004).

63. Saenko, O. A., Fyfe, J. C. & England, M. H. On the response of the oceanic wind-driven circulation to atmospheric CO2 increase. *Clim. Dyn.* **25**, 415–426 (2005).

64. Son, S.-W., Tandon, N. F., Polvani, L. M. & Waugh, D. W. Ozone hole and Southern Hemisphere climate change. *Geophys. Res. Lett.* https://doi.org/10.1029/2009GL038671 (2009).

65. Polvani, L. M., Waugh, D. W., Correa, G. J. & Son, S.-W. Stratospheric ozone depletion: The main driver of twentieth-century atmospheric circulation changes in the Southern Hemisphere. *J. Clim.* **24**, 795–812 (2011).

66. Thompson, D. W. et al. Signatures of the Antarctic ozone hole in Southern Hemisphere surface climate change. *Nat. Geosci.* **4**, 741–749 (2011).

67. Schneider, W. et al. Spin-up of South Pacific subtropical gyre freshens and cools the upper layer of the eastern South Pacific Ocean. *Geophys. Res. Lett.* https://doi.org/10.1029/2007GL031933 (2007).

68. Roemmich, D. et al. Decadal spinup of the South Pacific subtropical gyre. *J. Phys. Oceanogr.* **37**, 162–173 (2007).

69. Roemmich, D., Gilson, J., Sutton, P. & Zilberman, N. Multidecadal change of the South Pacific gyre circulation. *J.Phys. Oceanogr.* **46**, 1871–1883 (2016).

70. Zhang, X., Church, J. A., Platten, S. M. & Monselesan, D. Projection of subtropical gyre circulation and associated sea level changes in the Pacific based on CMIP3 climate models. *Clim. Dyn.* **43**, 131–144 (2014).

71. Zhai, F., Hu, D., Wang, Q. & Wang, F. Long-term trend of Pacific South Equatorial Current bifurcation over 1950–2010. *Geophys. Res. Lett.* **41**, 3172–3180 (2014).

72. Zhang, L. & Qu, T. Low-frequency variability of the South Pacific Subtropical Gyre as seen from satellite altimetry and Argo. *J. Phys. Oceanogr.* **45**, 3083–3098 (2015).

73. Hu, D. et al. Pacific western boundary currents and their roles in climate. *Nature* **522**, 299–308 (2015).

74. Alory, G., Wijffels, S. & Meyers, G. Observed temperature trends in the Indian Ocean over 1960–1999 and associated mechanisms. *Geophys. Res. Lett.* https://doi.org/10.1029/2006GL028044 (2007).

75. Biastoch, A., Böning, C. W., Schwarzkopf, F. U. & Lutjeharms, J. R. E. Increase in Agulhas leakage due to poleward shift of Southern Hemisphere westerlies. *Nature* **462**, 495–498 (2009).

76. Rouault, M., Penven, P. & Pohl, B. Warming in the Agulhas Current system since the 1980's. *Geophys. Res. Lett.* https://doi.org/10.1029/2009GL037987 (2009).

77. Beal, L. M., De Ruijter, W. P., Biastoch, A. & Zahn, R. On the role of the Agulhas system in ocean circulation and climate. *Nature* **472**, 429–436 (2011).

78. Durgadoo, J. V., Loveday, B. R., Reason, C. J., Penven, P. & Biastoch, A. Agulhas leakage predominantly responds to the Southern Hemisphere westerlies. *J. Phys. Oceanogr.* **43**, 2113–2131 (2013).

79. Cai, W., Shi, G., Cowan, T., Bi, D. & Ribbe, J. The response of the Southern Annular Mode, the East Australian Current, and the southern mid-latitude ocean circulation to global warming. *Geophys. Res. Lett.* https://doi.org/10.1029/2005GL024701 (2005).

80. Cai, W. Antarctic ozone depletion causes an intensification of the Southern Ocean super-gyre circulation. *Geophys. Res. Lett.* https://doi.org/10.1029/2005GL024911 (2006).

81. Li, W. et al. Intensification of the Southern Hemisphere summertime subtropical anticyclones in a warming climate. *Geophys. Res. Lett.* **40**, 5959–5964 (2013).

82. Wang, G., Cai, W. & Purich, A. Trends in Southern Hemisphere wind-driven circulation in CMIP5 models over the 21st century: Ozone recovery versus greenhouse forcing. *J. Geophys. Res.: Oceans* **119**, 2974–2986 (2014).

83. Wu, L. et al. Enhanced warming over the global subtropical western boundary currents. *Nat. Clim. Change* **2**, 161–166 (2012).

84. Ridgway, K. & Dunn, J. Observational evidence for a Southern Hemisphere oceanic supergyre. *Geophys. Res. Lett.* https://doi.org/10.1029/2007GL030392 (2007).

85. Roemmich, D. Super spin in the southern seas. *Nature* **449**, 34–35 (2007).

86. Arblaster, J. M., Meehl, G. A. & Karoly, D. J. Future climate change in the Southern Hemisphere: Competing effects of ozone and greenhouse gases. *Geophys. Res. Lett.* https://doi.org/10.1029/2010GL045384 (2011).

87. Deser, C. Certain uncertainty: The role of internal climate variability in projections of regional climate change and risk management. *Earth's Future* **8**, e2020EF001854 (2020).

88. Seager, R. & Simpson, I. R. Western boundary currents and climate change. *J. Geophys. Res.: Oceans* **121**, 7212–7214 (2016).

89. Marshall, G. J. et al. Causes of exceptional atmospheric circulation changes in the Southern Hemisphere. *Geophys. Res. Lett.* https://doi.org/10.1029/2004GL019952 (2004).

90. Oliver, E. & Holbrook, N. Extending our understanding of South Pacific gyre "spin-up": Modeling the East Australian Current in a future climate. *J. Geophys. Res.: Oceans* **119**, 2788–2805 (2014).

91. Yang, H. et al. Intensification and poleward shift of subtropical western boundary currents in a warming climate. *J. Geophys. Res.: Oceans* **121**, 4928–4945 (2016).

92. Yang, H. et al. Poleward shift of the major ocean gyres detected in a warming climate. *Geophys. Res. Lett.* **47**, e2019GL085868 (2020).

93. Qu, T., Fukumori, I. & Fine, R. A. Spin-up of the southern hemisphere super gyre. *J. Geophys. Res.: Oceans* **124**, 154–170 (2019).

94. Pontes, G., Gupta, A. S. & Taschetto, A. Projected changes to South Atlantic boundary currents and confluence region in the CMIP5 models: the role of wind and deep ocean changes. *Environ. Res. Lett.* **11**, 094013 (2016).

95. Marcello, F., Wainer, I. & Rodrigues, R. R. South Atlantic Subtropical Gyre late twentieth century changes. *J. Geophys. Res.: Oceans* **123**, 5194–5209 (2018).

96. Drouin, K. L., Lozier, M. S. & Johns, W. E. Variability and trends of the South Atlantic subtropical gyre. *J. Geophys. Res.: Oceans* **126**, e2020JC016405 (2021).

97. Sen Gupta, A. et al. Future changes to the Indonesian Throughflow and Pacific circulation: The differing role of wind and deep circulation changes. *Geophys. Res. Lett.* **43**, 1669–1678 (2016).

98. Gupta, A. S. et al. Future changes to the upper ocean Western Boundary Currents across two generations of climate models. *Scientific reports* **11**, 1–12 (2021).

99. Goyal, R., Sen Gupta, A., Jucker, M. & England, M. H. Historical and projected changes in the Southern Hemisphere surface westerlies. *Geophys. Res.Lett.* **48**, e2020GL090849 (2021).

100. Deng, K. et al. Changes of Southern Hemisphere westerlies in the future warming climate. *Atmos. Res.* https://doi.org/10.1016/j.atmosres.2022.106040 (2022).

101. Lique, C. & Thomas, M. D. Latitudinal shift of the Atlantic Meridional Overturning Circulation source regions under a warming climate. *Nature Climate Change* **8**, 1013–1020 (2018).

102. Garzoli, S. L., Baringer, M. O., Dong, S., Perez, R. C. & Yao, Q. South Atlantic meridional fluxes. *Deep Sea Res. Part I: Oceanogr. Res. Papers* **71**, 21–32 (2013).

103. Zhu, C. & Liu, Z. Weakening Atlantic overturning circulation causes South Atlantic salinity pile-up. *Nat. Clim. Change* **10**, 998–1003 (2020).

104. Blunden, J. & Arndt, D. State of the Climate in 2019. *Bullet. Am. Meteorol. Soc.* **101**, S1–S429 (2020).

105. Biastoch, A. & Böning, C. W. Anthropogenic impact on Agulhas leakage. *Geophys. Res. Lett.* **40**, 1138–1143 (2013).

106. Kay, J. E. et al. The Community Earth System Model (CESM) large ensemble project: A community resource for studying climate change in the presence of internal climate variability. *Bullet. Am. Meteorol. Soc.* **96**, 1333–1349 (2015).

107. Schwalm, C. R., Glendon, S. & Duffy, P. B. RCP8. 5 tracks cumulative CO2 emissions. *Proc. Natl Acad. Sci. USA* **117**, 19656–19657 (2020).

108. Deser, C. et al. Insights from Earth system model initial-condition large ensembles and future prospects. *Nat. Clim. Change* **10**, 277–286 (2020).

109. Williams, R. G. & Follows, M. J. *Ocean Dynamics and the Carbon Cycle: Principles and Mechanisms* (Cambridge University Press, 2011).

110. Signorini, S. R. & McClain, C. R. Subtropical gyre variability as seen from satellites. *Remote Sens. Lett.* **3**, 471–479 (2012).

111. Yamamoto, A. et al. Roles of the ocean mesoscale in the horizontal supply of mass, heat, carbon, and nutrients to the Northern Hemisphere subtropical gyres. *J. Geophys. Res.: Oceans* **123**, 7016–7036 (2018).

112. Jamet, Q., Deremble, B., Wienders, N., Uchida, T. & Dewar, W. On wind-driven energetics of subtropical gyres. *J. Adv. Model. Earth Syst.* **13**, e2020MS002329 (2021).

113. Gupta, M. et al. A nutrient relay sustains subtropical ocean productivity. *Proc. Natl Acad. Sci. USA* **119**, e2206504119 (2022).

114. Weijer, W., De Ruijter, W. P., Sterl, A. & Drijfhout, S. S. Response of the Atlantic overturning circulation to South Atlantic sources of buoyancy. *Global and Planetary Change* **34**, 293–311 (2002).

115. Knorr, G. & Lohmann, G. Southern Ocean origin for the resumption of Atlantic thermohaline circulation during deglaciation. *Nature* **424**, 532–536 (2003).

116. Cimatoribus, A. A., Drijfhout, S. S., Den Toom, M. & Dijkstra, H. A. Sensitivity of the Atlantic meridional overturning circulation to South Atlantic freshwater anomalies. *Clim. Dyn.* **39**, 2291–2306 (2012).

117. Boebel, O. et al. The intermediate depth circulation of the western South Atlantic. *Geophys. Res, Lett.* **26**, 3329–3332 (1999).

118. Rodrigues, R. R., Wimbush, M., Watts, D. R., Rothstein, L. M. & Ollitrault, M. South Atlantic mass transports obtained from subsurface float and hydrographic data. *J. Marine Res.* **68**, 819–850 (2010).

119. Marcello, F., Wainer, I., Gent, P. R., Otto-Bliesner, B. L. & Brady, E. C. South Atlantic Surface Boundary Current System during the Last Millennium in the CESM-LME: The Medieval Climate Anomaly and Little Ice Age. *Geosciences* **9**, 299 (2019).

120. Richardson, P. L. Agulhas leakage into the Atlantic estimated with subsurface floats and surface drifters. *Deep Sea Res. Part I: Oceanogr. Res. Papers* **54**, 1361–1389 (2007).

121. Stramma, L. Geostrophic transport of the South Equatorial Current in the Atlantic. *J. Marine Res.* **49**, 281–294 (1991).

122. Schmid, C. Mean vertical and horizontal structure of the subtropical circulation in the South Atlantic from three-dimensional observed velocity fields. *Deep Sea Res. Part I: Oceanogr. Res. Papers* **91**, 50–71 (2014).

123. Luko, C., da Silveira, I., Simoes-Sousa, I., Araujo, J. & Tandon, A. Revisiting the Atlantic South Equatorial Current. *J. Geophys. Res.: Oceans* **126**, e2021JC017387 (2021).

124. Schmid, C. & Majumder, S. Transport variability of the Brazil Current from observations and a data assimilation model. *Ocean Sci.* **14**, 417–436 (2018).

125. Lumpkin, R. & Garzoli, S. L. Near-surface circulation in the tropical Atlantic Ocean. *Deep Sea Res. Part I: Oceanogr. Res. Papers* **52**, 495–518 (2005).

126. Rocha, C. B., da Silveira, I. C., Castro, B. M. & Lima, J. A. M. Vertical structure, energetics, and dynamics of the Brazil Current System at 22 S–28 S. *J. Geophys. Res.: Oceans* **119**, 52–69 (2014).

127. Pedlosky, J. The dynamics of the oceanic subtropical gyres. *Science* **248**, 316–322 (1990).

128. Tsuchiya, M., Talley, L. D. & McCartney, M. S. Water-mass distributions in the western South Atlantic; A section from South Georgia Island (54S) northward across the equator. *J. Marine Res.* **52**, 55–81 (1994).

129. Stramma, L. & Schott, F. The mean flow field of the tropical Atlantic Ocean. *Deep Sea Res. Part II: Topical Studies in Oceanogr.* **46**, 279–303 (1999).

130. Munk, W. H. On the wind-driven ocean circulation. *J. Atmos. Sci.* **7**, 80–93 (1950).

131. Sverdrup, H. U. Wind-driven currents in a baroclinic ocean; with application to the equatorial currents of the eastern Pacific. *Proc. Natl Acad. Sci. USA* **33**, 318–326 (1947).
132. Stommel, H. The westward intensification of wind-driven ocean currents. *Eos, Transactions Am. Geophys. Union* **29**, 202–206 (1948).
133. Vallis, G. K. *Climate and the Oceans* (Princeton University Press, 2011).
134. Wells, N. C. *Encyclopedia of Ocean Sciences* 3rd Edn (Academic Press, 2017).
135. Fogt, R. L. & Marshall, G. J. The Southern Annular Mode: variability, trends, and climate impacts across the Southern Hemisphere. *Wiley Interdisciplinary Rev.: Clim. Change* **11**, e652 (2020).
136. Hall, A. & Visbeck, M. Synchronous variability in the Southern Hemisphere atmosphere, sea ice, and ocean resulting from the annular mode. *J. Clim.* **15**, 3043–3057 (2002).
137. Fyfe, J. C. & Saenko, O. A. Simulated changes in the extratropical Southern Hemisphere winds and currents. *Geophys. Res. Lett.* https://doi.org/10.1029/2005GL025332 (2006).
138. Wang, Z., Kuhlbrodt, T. & Meredith, M. On the response of the Antarctic Circumpolar Current transport to climate change in coupled climate models. *J. Geophys. Res.: Oceans* https://doi.org/10.1029/2010JC006757 (2011).
139. Thomas, M. D., De Boer, A. M., Johnson, H. L. & Stevens, D. P. Spatial and temporal scales of Sverdrup balance. *J. Phys. Oceanogr.* **44**, 2644–2660 (2014).
140. Yeager, S. Topographic coupling of the Atlantic overturning and gyre circulations. *J. Phys. Oceanogr.* **45**, 1258–1284 (2015).
141. Thomas, M., de Boer, A. M., Stevens, D. & Johnson, H. Upper ocean manifestations of a reducing meridional overturning circulation. *Geophys. Res. Lett.* https://doi.org/10.1029/2012GL052702 (2012).
142. Jones, C. S. & Cessi, P. Interbasin transport of the meridional overturning circulation. *J. Phys. Oceanogr.* **46**, 1157–1169 (2016).
143. Stommel, H. A survey of ocean current theory. *Deep Sea Res.* **4**, 149–184 (1957).
144. Qiu, B. & Chen, S. Decadal variability in the large-scale sea surface height field of the South Pacific Ocean: Observations and causes. *J. Phys. Oceanogr.* **36**, 1751–1762 (2006).
145. Qiu, B. & Chen, S. Multidecadal sea level and gyre circulation variability in the northwestern tropical Pacific Ocean. *J. Phys. Oceanogr.* **42**, 193–206 (2012).
146. Foukal, N. P. & Lozier, M. S. Assessing variability in the size and strength of the N orth A tlantic subpolar gyre. *J. Geophys. Res.: Oceans* **122**, 6295–6308 (2017).
147. Cheng, W., Chiang, J. C. & Zhang, D. Atlantic meridional overturning circulation (AMOC) in CMIP5 models: RCP and historical simulations. *J. Clim.* **26**, 7187–7197 (2013).
148. Schleussner, C.-F., Levermann, A. & Meinshausen, M. Probabilistic projections of the Atlantic overturning. *Clim. Change* **127**, 579–586 (2014).
149. Weijer, W., De Ruijter, W. P. & Dijkstra, H. A. Stability of the Atlantic overturning circulation: Competition between Bering Strait freshwater flux and Agulhas heat and salt sources. *J. Phys. Oceanogr.* **31**, 2385–2402 (2001).
150. Polo, I., Robson, J., Sutton, R. & Balmaseda, M. A. The importance of wind and buoyancy forcing for the boundary density variations and the geostrophic component of the AMOC at 26 N. *J. Phys. Oceanogr.* **44**, 2387–2408 (2014).
151. Timmermann, A. & Goosse, H. Is the wind stress forcing essential for the meridional overturning circulation? *Geophys. Res. Lett.* https://doi.org/10.1029/2003GL018777 (2004).
152. Weijer, W., De Ruijter, W. P., Dijkstra, H. A. & Van Leeuwen, P. J. Impact of interbasin exchange on the Atlantic overturning circulation. *J. Phys. Oceanogr.* **29**, 2266–2284 (1999).
153. Rahmstorf, S. On the freshwater forcing and transport of the Atlantic thermohaline circulation. *Clim. Dyn.* **12**, 799–811 (1996).
154. Kostov, Y. et al. Distinct sources of interannual subtropical and subpolar Atlantic overturning variability. *Nat. Geosci.* **14**, 491–495 (2021).
155. Muglia, J. & Schmittner, A. Glacial Atlantic overturning increased by wind stress in climate models. *Geophys. Res. Lett.* **42**, 9862–9868 (2015).
156. Rahmstorf, S. In *Encyclopedia of Quaternary Science* 5 (Elsevier, 2006).
157. Johnson, H. L., Cessi, P., Marshall, D. P., Schloesser, F. & Spall, M. A. Recent contributions of theory to our understanding of the Atlantic meridional overturning circulation. *J. Geophy. Res.: Oceans* **124**, 5376–5399 (2019).
158. Joos, F. & Spahni, R. Rates of change in natural and anthropogenic radiative forcing over the past 20,000 years. *Proc. Natl Acad. Sci. USA* **105**, 1425–1430 (2008).
159. Gruber, N. et al. The oceanic sink for anthropogenic CO2 from 1994 to 2007. *Science* **363**, 1193–1199 (2019).
160. Ciais, P. et al. In *Climate Change 2013: The Physical Science Basis. Contribution of Working Group I to the Fifth Assessment Report of the Intergovernmental Panel on Climate Change* 465–570 (Cambridge University Press, 2014).
161. Morrison, A. K., Griffies, S. M., Winton, M., Anderson, W. G. & Sarmiento, J. L. Mechanisms of Southern Ocean heat uptake and transport in a global eddying climate model. *J. Clim.* **29**, 2059–2075 (2016).
162. Shi, J.-R., Xie, S.-P. & Talley, L. D. Evolving relative importance of the Southern Ocean and North Atlantic in anthropogenic ocean heat uptake. *J. Clim.* **31**, 7459–7479 (2018).
163. Pérez, F. F. et al. Atlantic Ocean CO 2 uptake reduced by weakening of the meridional overturning circulation. *Nat. Geosci.* **6**, 146–152 (2013).
164. Rosón, G., Ríos, A. F., Pérez, F. F., Lavín, A. & Bryden, H. L. Carbon distribution, fluxes, and budgets in the subtropical North Atlantic Ocean (24.5 N). *J. Geophys. Res.: Oceans* https://doi.org/10.1029/1999JC000047 (2003).
165. Steinfeldt, R., Rhein, M., Bullister, J. L. & Tanhua, T. Inventory changes in anthropogenic carbon from 1997–2003 in the Atlantic Ocean between 20 S and 65 N. *Global Biogeochem. Cycles* https://doi.org/10.1029/2008GB003311 (2009).
166. Palter, J. B. & Lozier, M. S. On the source of Gulf Stream nutrients. *J. Geophys. Res.: Oceans* https://doi.org/10.1029/2007JC004611 (2008).
167. DeVries, T., Holzer, M. & Primeau, F. Recent increase in oceanic carbon uptake driven by weaker upper-ocean overturning. *Nature* **542**, 215–218 (2017).
168. Zanna, L., Khatiwala, S., Gregory, J. M., Ison, J. & Heimbach, P. Global reconstruction of historical ocean heat storage and transport. *Proc. Natl Acad. Sci. USA* **116**, 1126–1131 (2019).
169. Bronselaer, B. & Zanna, L. Heat and carbon coupling reveals ocean warming due to circulation changes. *Nature* **584**, 227–233 (2020).
170. Winton, M., Griffies, S. M., Samuels, B. L., Sarmiento, J. L. & Frölicher, T. L. Connecting changing ocean circulation with changing climate. *J. Clim.* **26**, 2268–2278 (2013).
171. Heinze, C. et al. The quiet crossing of ocean tipping points. *Proc. Natl Acad. Sci. USA* **118**, e2008478118 (2021).
172. Hurrell, J. W. et al. The Community Earth System Model: a framework for collaborative research. *Bullet. Am. Meteorol. Soc.* **94**, 1339–1360 (2013).
173. Deser, C., Phillips, A. S., Alexander, M. A. & Smoliak, B. V. Projecting North American climate over the next 50 years: Uncertainty due to internal variability. *J. Clim.* **27**, 2271–2296 (2014).
174. Solomon, S., Manning, M., Marquis, M., Qin, D. et al. *Climate Change 2007-the Physical Science Basis: Working Group I Contribution to the Fourth Assessment Report of the IPCC* Vol. 4 (Cambridge University Press, 2007).
175. Mann, H. B. Nonparametric tests against trend. *J. Econom. Soc.* **13**, 245–259 (1945).
176. Kendall, M. G. *Rank Correlation Methods* (Griffin, 1948).
177. Lee Rodgers, J. & Nicewander, W. A. Thirteen ways to look at the correlation coefficient. *Am. Stat.* **42**, 59–66 (1988).

Acknowledgements

Author contributions

F.M. designed the study, performed the analysis, made the figures and wrote the paper. M.T. discussed methods, contributed to the interpretation of model results and helped revise the manuscript. B.F. helped with the acquisition and pre-processing of the 40 CESM1-LE members. I.W. helped with the conceptualization of the manuscript, provided the infrastructure needed for carrying out the numerical experiments and supervised the work. All the authors contributed with ideas, discussed the results and contributed to the text.

Competing interests

The authors declare no competing interests.

Additional information

Supplementary information The online version contains supplementary material available at https://doi.org/10.1038/s43247-023-00750-4.

Correspondence and requests for materials should be addressed to Fernanda Marcello.

Peer review information *Communications Earth & Environment* thanks the anonymous reviewers for their contribution to the peer review of this work. Primary Handling Editors: Regina Rodrigues, Joe Aslin and Heike Langenberg. Peer reviewer reports are available.

Reprints and permission information is available at http://www.nature.com/reprints

Publisher's note Springer Nature remains neutral with regard to jurisdictional claims in published maps and institutional affiliations.